Article | Open Access

Energy Materials

Chen et al. Energy Mater. 2026, 6, 600089 DOI:10.20517/energymater.2026.102

Reconstructing the perovskite surface with a homogeneous electric potential by reducing localized charge for efficient and durable perovskite solar cells

Runhao Chen[1], Jiankai Zhang[1,*], Yi Luo[1], Zebin Guo[1], Wenyi Wu[1], Xin Xu[2,*], Chengwen Huang[3,*], Hai Zhou[1,*]

Keywords:
Perovskite solar cells, non-radiative recombination, localized charges, surface potential, (ferrocenylmethyl)trimethyl ammonium chloride

Citation: Chen, R.; Zhang, J.; Luo, Y.; Guo, Z.; Wu, W.; Xu, X.; Huang, C.; Zhou, H. Reconstructing the perovskite surface with a homogeneous electric potential by reducing localized charge for efficient and durable perovskite solar cells. *Energy Mater.* **2026**, *6*, 600089. https://dx.doi.org/10.20517/energymater.2026.102

Received: 30 Apr 2026
First Decision: 12 Jun 2026
Revised: 29 Jun 2026
Accepted: 17 Jul 2026
Published: 31 Jul 2026

Academic Editor: Yuping Wu
Copy Editor: Ping Zhang
Production Editor: Ping Zhang

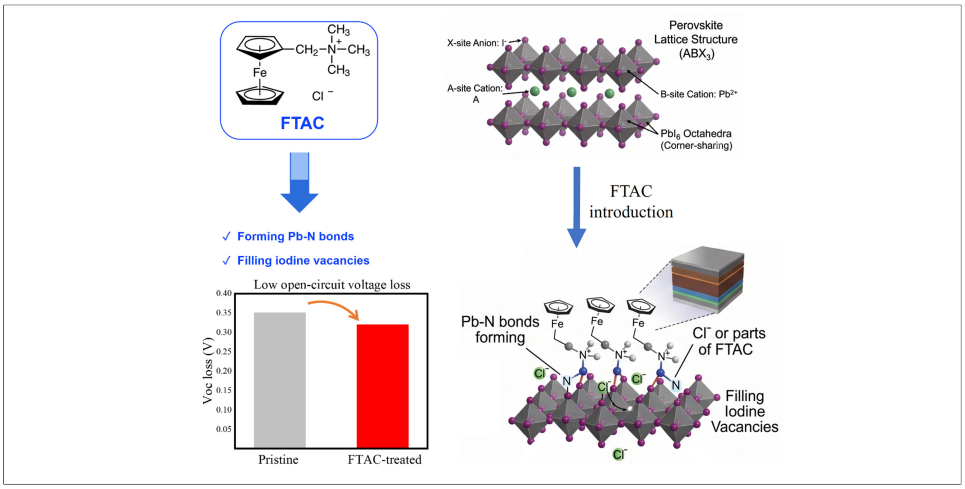

Abstract

The non-radiative recombination induced by localized charges and inhomogeneous surface potential of perovskite film limits the advancement of stable and efficient perovskite solar cells (PSCs). Herein, for the first time, (Ferrocenylmethyl)trimethylammonium chloride (FTAC) is introduced to reconstruct the surface of the perovskite film. Calculations reveal Pb-N coordination between FTAC and the perovskite framework, accompanied by iodine-vacancy compensation, thereby leading to effective defect passivation and mitigating charge localization. Meanwhile, this reconstruction strategy ensures potential uniformity across the perovskite interface and a more p-type characteristic, thereby accelerating the charge transport in PSCs. As a result, FTAC-modified devices deliver an outstanding efficiency of 25.06% with a low voltage deficit of 0.32 V, a significant improvement over the 23.31% efficiency of control PSCs. In addition, the target devices display excellent stability, retaining 91.16% of their initial efficiency after 1,000 h aging at 85 °C in N_2 and 88.67% after 1,000 h of continuous maximum power point tracking at 65 °C. In the

[1]School of Integrated Circuits, Dongguan University of Technology, Dongguan 523808, Guangdong, China.
[2]DGUT-CNAM Institute, Dongguan University of Technology, Dongguan 523808, Guangdong, China.
[3]School of Optoelectronic Engineering, Guilin University of Electronic Technology, Guilin 541004, Guangxi, China.

***Correspondence to:** Dr. Jiankai Zhang, Prof. Hai Zhou, School of Integrated Circuits, Dongguan University of Technology, Dongguan 523808, Guangdong, China. E-mail: jkzhang; hizhou@dgut.edu.cn; Dr. Xin Xu, DGUT-CNAM Institute, Dongguan University of Technology, Dongguan 523808, Guangdong, China. E-mail: xuxin@dgut.edu.cn; Dr. Chengwen Huang, School of Optoelectronic Engineering, Guilin University of Electronic Technology, Guilin 541004, Guangxi, China. E-mail: cwhuang@guet.edu.cn

present study, by reconstructing the perovskite film surface to achieve a homogeneous potential distribution, non-radiative recombination is effectively reduced, offering an innovative approach to boost PSC efficiency and device stability.

INTRODUCTION

Following their initial discovery in 2009, perovskite solar cells (PSCs) have attracted considerable attention owing to their outstanding optoelectronic properties[1], inexpensive solution process[4,5], and sequential improvements in power conversion efficiency (PCE)[6]. Currently, the certified PCE of monolithic PSCs has now exceeded 27%[9], surpassing the performance of many crystalline-silicon photovoltaic modules. Nevertheless, localized charges induced by massive defects and the non-uniform surface potential of perovskite layers remain key contributors to non-radiative recombination, which hinders the advancement of n-i-p structured PSCs[10]. Thus, effective optimization strategies are urgently needed to address these challenges.

The generation of local charges on the perovskite surface is mainly related to the intrinsic crystal defects and the inevitable surface defects during the perovskite film fabrication process[14]. The large number of localized charges at the interface leads to an inhomogeneous surface electric potential distribution, which subsequently triggers severe non-radiative recombination across the perovskite-hole transport layer (HTL) interface. In recent years, various studies have proposed some methods (such as additive engineering and post-deposition treatments) to address the surface trap states and localized charge issues of perovskite films[15]. For instance, Shi *et al.* added indene-C60 bisadduct nanoparticles into the perovskite inks, which modulated perovskite crystallization and achieved holistic bulk film passivation by passivating defects in the interiors of perovskite films. The corresponding blade-coated devices achieved impressive PCE and operational stability due to the reduction of defects and localized charges[18]. In addition, Zhang *et al.* found that the incorporation of pseudo-halogen thiocyanate ions in perovskite can occupy iodine vacancies and suppress halide-ion migration through steric hindrance effects, which greatly reduces energy loss and improves the operational stability[19]. In addition to additive engineering, post-treatment of the perovskite surface with surface passivators is also an effective strategy to reduce surface defects and localized charges[20]. Pan *et al.* used ethylene diammonium diiodide to heal halide and organic-cation vacancies at the perovskite interface, thereby suppressing non-radiative recombination and achieving a certified PCE of 28.49% in tandem devices[23]. In another study, the active layer surface was reconstructed by Zhu *et al.* with a dual-layer heterojunction architecture, which reduces the trap density near the perovskite/C60 interface by an order of magnitude, achieves low open-circuit voltage (V_{oc}) loss, and achieves an impressive PCE over 26%[24]. These strategies provide valuable insights for surface defects in perovskite films. Even so, the connections between surface defect states, local charge distribution, and surface potential in perovskite films remain poorly elucidated, and gaining such insight would help improve charge transfer and limit non-radiative recombination in PSCs.

In addition to the localized charges caused by defects, the nonuniform surface electric potential also constitutes a cornerstone of determining the performance and stability of PSCs, as it directly affects the processes of charge separation, transport, and recombination at the interfaces[25,26]. The uniform surface potential of perovskite films can facilitate balanced carrier extraction into adjacent charge-selective layers, preventing excessive interfacial charge accumulation and consequently suppressing recombination losses[27]. A multifunctional ionic liquid, 1-allyl-3-methylimidazole dicyanamide, was employed by Xu *et al.* as an additive in the precursor to regulate surface potential, leading to reduced non-radiative recombination and improved photovoltaic performance and stability[28]. Huang *et al.* developed a bifacial surface potential regulation strategy through interface doping, which effectively promotes interfacial charge carrier extraction

and suppresses carrier recombination. As a consequence, the optimized PSCs achieved the highest PCE of 26.05% and impressive stability[29].

These pioneering works demonstrate that reducing defect density can alleviate local charge buildup, leading to a more homogeneous surface potential and consequently lower non-radiative recombination. Nevertheless, we hope to formulate a simple and efficient scheme that can simultaneously reduce the localized carriers at the perovskite interface and improve the uniformity of the surface potential. Ferrocene is a highly electron-rich system composed of two cyclopentadiene rings embedded with iron ions, which endows it with excellent charge transfer capability[30,31]. The highest occupied molecular orbital (HOMO) of ferrocene derivatives can be precisely engineered through chemical modification of the cyclopentadienyl ring with various functional groups, thereby making them ideal interlayers for PSCs[32,33].

In this work, (Ferrocenylmethyl)trimethylammonium chloride (FTAC) is first combined with dimethyl sulfoxide (DMSO) to reconstruct the upper surface of the perovskite film. A small amount of DMSO can dissolve the components with relatively weak chemical bonds on the surface of the perovskite, thereby providing active sites for the formation of Pb-N bonds between FTA^+ and perovskite. Theoretical and experimental results indicate that FTAC passivates defects by coordinating with undercoordinated Pb^{2+} via Pb-N interactions, accompanied by iodine-vacancy healing. Meanwhile, the surface reconstruction strategy boosts the perovskite film crystallinity, reduces localized charges caused by surface defects, enhances the uniform distribution of surface potential across the perovskite layer while refining energy level alignment at its interface with the HTL. Consequently, the highest PCE of 25.06%, with a low open-circuit voltage loss of 0.32 V, is achieved due to the reduction of non-radiative recombination. Furthermore, the stability of modified PSCs is enhanced by this surface reconstruction strategy, which toughens the upper surface of the perovskite film. This work introduces a new method of facile surface reconstruction that enables enhanced efficiency and stability in PSCs.

EXPERIMENTAL

Materials

Indium tin oxide (ITO)-coated glass substrates (sheet resistance ≈15 Ω/sq) were supplied by China Southern Glass (CSG) Holding Co., Ltd. PbI_2 (99.99%) was purchased from Advanced Election Technology CO., Ltd. Formamidinium iodide (FAI) (99.5%), methylammonium iodide (MAI) (99.5%), methylammonium chloride (MACL) (99.5%), [6,6]-phenyl-C61-butyric acid methyl ester (PCBM) and 2,2',7,7'-tetrakis[N,N-di(4-methoxyphenyl)amino]-9,9'-spirobifluorene (spiro-OMeTAD) (99.8%) were obtained from Xi'an Polymer Light Technology Corp. Isopropanol (IPA) (99.5%) and (Ferrocenylmethyl)trimethylammonium chloride (95%) were purchased from Aladdin. N,N-dimethylformamide (DMF) (99%) and chlorobenzene (CB) (99.9%) were purchased from Sigma-Aldrich. DMSO (99%) and SnO_2 colloid were purchased from Alfa Aesar. All materials used in this work are commercially available and were used as received without additional synthesis or purification unless otherwise stated. In particular, FTAC was obtained from Aladdin Biochemical Technology Co., Ltd., avoiding complex molecular synthesis and purification procedures. Given that FTAC was only used at a low concentration of 0.05-0.2 mg/mL for surface treatment, the additional material consumption and cost are limited. Regarding safety and toxicity, lead salts and organic solvents were handled according to the corresponding safety data sheets with appropriate personal protective equipment in a glovebox or fume hood, and FTAC was also handled following the supplier-provided safety information.

Device fabrication

Sequential ultrasonic cleaning was performed on the etched ITO substrates using deionized water, isopropanol, and anhydrous ethanol, each for 15 min. The pre-cleaned substrates were then exposed to UV-ozone for 15 min to eliminate residual organic contaminants and improve surface wettability. Spin coating

was used to deposit the SnO_2 layer onto ITO at 4,000 rpm for 30 s, after which the film was annealed at 150 °C for 10 min in air (colloidal SnO_2 diluted with deionized water at a 1:4 volume ratio). The substrates were subsequently subjected to UV-ozone treatment for 15 min after cooling to room temperature. The substrates were promptly transferred into the glovebox thereafter. The 1.50 M PbI_2 precursor solution was dissolved in DMF and DMSO (volume ratio of 9:1). A mixed organic salt precursor solution was prepared by dissolving FAI (0.52 M), MAI (0.040 M), and MACl (0.13 M) in IPA (total volume: 2.2 mL). Spin coating was used to form PbI_2 films on SnO_2 substrates (4,000 rpm, 30 s), after which the films were annealed at 70 °C for 1 min. Spin coating was used to apply the mixed organic salt precursor onto the PbI_2 (1,500 rpm, 30 s). Afterward, the samples were annealed at 100 °C for 50 min in a nitrogen atmosphere in a glovebox. Prior to deposition of the hole transport layer, the FTAC solution (prepared in IPA/DMSO, 200:1 v/v) was applied by spin coating at 5,000 rpm for 30 s and then annealed at 100 °C for 5 min. Subsequently, the Spiro-OMeTAD solution was deposited via spin coating at 4,000 rpm for 30 s to form the hole transport layer. Ultimately, thermal evaporation was employed to deposit an 80 nm Ag top contact under a vacuum of $5*10^{-4}$ Pa. The defined active area for the resulting devices was 0.09 cm^2. In the case of electron-only devices, the perovskite surface was covered with a PCBM layer by spin-coating its chlorobenzene solution (20 mg/mL) at 4,000 rpm for 40 s.

Characterizations

Both the space-charge-limited current (SCLC) behavior and the illuminated current density-voltage (*J-V*) characteristics were acquired utilizing a Keithley 2450 system (Keithley Instruments/Tektronix, USA). To evaluate the photovoltaic performance, *J-V* sweeps were conducted using a calibrated AM 1.5G solar simulator (CEL-AAAS50, China Education Au-light Co., Ltd., China) with an irradiation intensity of 100 mW/cm^2. Characterizations of the surface topography and crystallographic properties of the perovskite layers were carried out utilizing a VeriosG4UC system (Thermo Fisher Scientific, USA). The X-ray photoelectron spectroscopy (XPS) and Ultraviolet photoelectron spectroscopy (UPS) spectra were measured using ESCALAB XI (Thermo Fisher Scientific, USA). A Cary 5000 spectrophotometer (Agilent Technologies, USA) was utilized to acquire the ultraviolet-visible-near-infrared (UV-Vis-NIR) absorption spectra. Steady-state photoluminescence (PL) and time-resolved photoluminescence (TRPL) data were acquired with an FLS-1000 fluorescence spectrometer (Edinburgh Instruments, UK). A D8 ADVANCE multifunctional X-ray diffractometer equipped (Bruker AXS, Germany) with a Cu Kα radiation source (40 kV and 40 mA) was utilized to record the X-ray diffraction (XRD) patterns. Atomic force microscopy (AFM) (Ntegra Prima, NTMDT) integrated with the Kelvin probe force microscopy (KPFM) mode was used to analyze the topography and surface potential [Ntegra Prima, Nanotechnology Molecular Devices and Tools (NT-MDT), Russia]. An SRF50 test system was utilized to acquire the external quantum efficiency (EQE) data. An Auto Lab PGSTAT 302N electrochemical workstation (Metrohm Autolab, the Netherlands) was utilized to acquire the capacitance-voltage (*C-V*) characteristics.

Calculation method

Theoretical calculations in this study were conducted based on density functional theory (DFT) methods. For all DFT simulations, the exchange-correlation potential was described utilizing the generalized gradient approximation (GGA) with the Perdew, Burke, and Ernzerhof (PBE) functional[34]. The calculations related to surface passivation were carried out using the Vienna Ab-initio Simulation Package (VASP)[35] code with the projector augmented wave method (PAW)[35,36] . A plane-wave basis set with a kinetic energy cutoff of 450 eV was utilized to solve the Kohn-Sham equations for all density functional theory calculations. For the Brillouin zone integration, a 2 × 2 × 1 Γ-centered k-point mesh was adopted. The atomic structures were optimized until the residual Hellmann-Feynman force on each atom dropped below 0.05 eV/A.

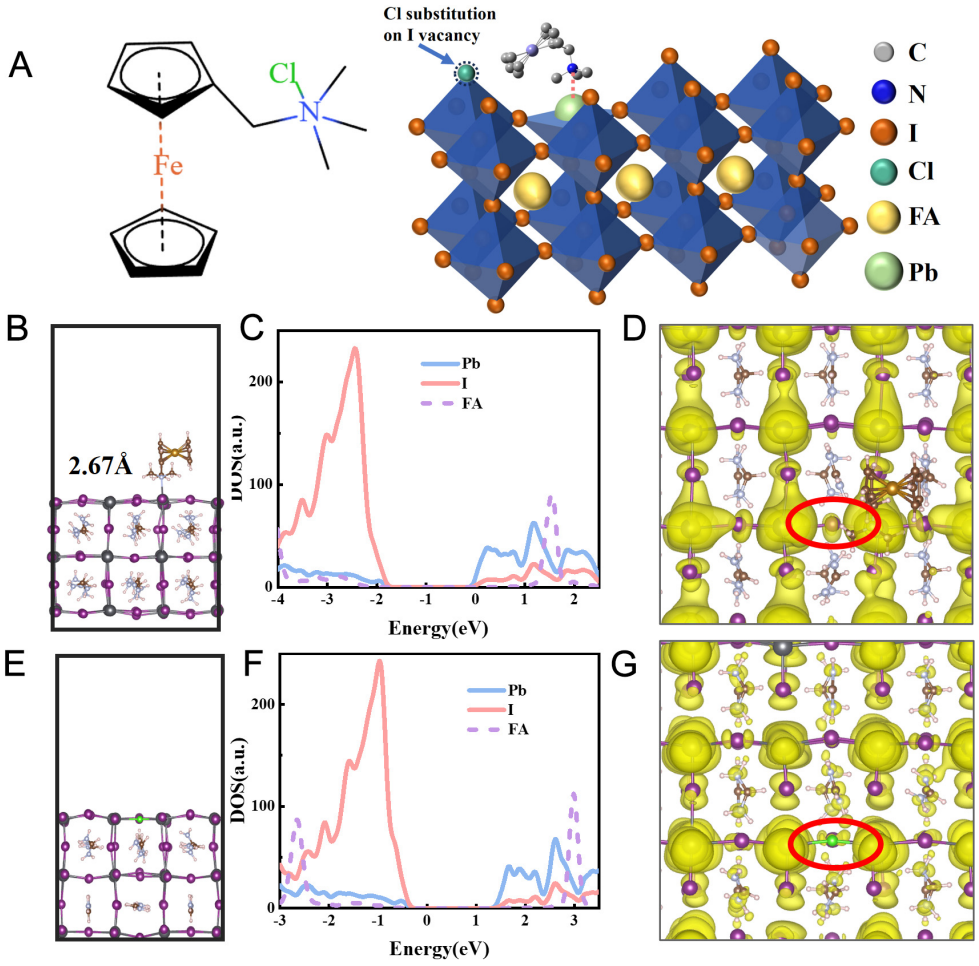

Figure 1. (A) The chemical structure of FTAC and a schematic diagram illustrating the function of FTAC on the surface of the perovskite film; (B) The passivated V_I-$FAPbI_3$ surface structure with FTA^+; (C) Density of states (DOS) for (B) systems, and the control group is shown in Supplementary Figure 3A. The DOS is referenced to the Fermi level of each system (set to 0 eV); (D) Charge density distribution of the (B) system; (E) The passivated V_I-$FAPbI_3$ surface structure with a Cl atom; (F) DOS for (E) systems; (G) Charge density distribution of the (E) system. FTAC: (Ferrocenylmethyl)trimethylammonium chloride; FTA: (ferrocenylmethyl)trimethylammonium cation.

RESULTS AND DISCUSSION

The structural characteristics of the FTAC molecule and a schematic diagram illustrating the function of FTAC at the perovskite film surface are shown in Figure 1A. The FTAC is anticipated to passivate surface defects in perovskite films via Pb-N coordination with undercoordinated Pb^{2+} and filling iodine vacancies. The perovskite layer was fabricated via a two-step deposition process, while FTAC was dissolved in an isopropanol (IPA)/DMSO solvent mixture (200:1), as shown in Supplementary Figure 1. To clarify whether the two-step process leads to a markedly A-site-rich surface, surface-sensitive XPS analysis was performed to compare the one-step and two-step-deposited perovskite films. As summarized in Supplementary Table 1, the N 1s atomic percentages of the one-step and two-step films are 13.09% and 12.46%, respectively, while the corresponding Pb $4f_{7/2}$/N 1s atomic ratios are 6.64 and 7.02 in Supplementary Table 2. These comparable values indicate that the two-step-processed film does not show a significantly higher surface A-site-related N content than the one-step film. Therefore, locally Pb-rich or undercoordinated Pb-containing surface regions can still exist in the two-step-processed perovskite film, supporting the use of a PbI_2-terminated surface model for the subsequent DFT calculations.

First-principles calculations based on DFT were performed to elucidate the passivation role of FTAC on the perovskite surface. For the DFT analysis, the PbI_2-terminated $FAPbI_3$ (001) surface was adopted as the representative model. The constructed surface model and the optimized adsorption configurations of FTAC on the perovskite surface are presented in Supplementary Figure 2. Although the FAI-terminated surface may be favorable in an idealized structure, it is considered less stable under realistic conditions because FA-related surface species are vulnerable to heat and moisture[37]. In contrast, the PbI_2-terminated surface is more likely to persist experimentally and generally shows stronger interaction with adsorbed molecules than the FAI-terminated surface[38]. Initially, an $FTA^+/FAPbI_3$ model was established. FTA^+ exhibits an adsorption energy of -0.87 eV on the surface, indicating that the thermodynamic interaction is favorable. This adsorption strength is attributed to the formation of a Pb-N dative bond, with a bond length of 2.67 Å [Figure 1B]. Furthermore, density of states (DOS) analysis was performed to elucidate how FTA^+ passivates the $FAPbI_3$ surface [Supplementary Figure 3A and Figure 1C]. The DOS plots are referenced to the Fermi level of each model and are therefore used here for qualitative comparison of defect-state suppression rather than direct comparison of absolute band-edge energies across different systems. Supplementary Figure 3A presents the DOS of V_I- $FAPbI_3$, where deep-level defect states arising from Pb-s orbitals appear near the Fermi level and act as Shockley-Read-Hall nonradiative recombination centers. As illustrated in Figure 1C, these defect states are fully suppressed upon the incorporation of FTA^+ on the V_I-$FAPbI_3$ surface. To elucidate the passivation mechanism, charge density distribution was analyzed. Supplementary Figure 3B shows a pronounced accumulation of electron density near the V_I defect on the $FAPbI_3$ (001) surface, indicating that V_I behaves as a donor-type defect. Following the introduction of FTA^+, the formation of Pb-N bonds effectively passivates these defect states, thereby decreasing carrier trapping and electron-hole recombination [Figure 1D]. Consequently, incorporating FTA^+ significantly reduces the density of interfacial defects on the perovskite film surface. In addition, Cl^- from the FTAC molecule occupies the V_I site and forms the Pb-Cl chemical bond on the perovskite surface. This Cl^- substitution contributes to vacancy-site defect compensation, which helps suppress defect states and reduce local charge localization [Figure 1E-G]. Overall, the results suggest that the passivation effect of FTAC arises from the complementary actions of its two components: FTA^+ mainly regulates the interfacial electronic environment through Pb-N coordination, while Cl^- mainly assists in healing V_I defects. As a result, FTAC effectively mitigates detrimental interfacial defects and alleviates localized charge accumulation at the contact interface between the perovskite absorber and the HTL.

Bonding interactions between FTAC and Pb^{2+} species in the perovskite layer were analyzed using XPS [Supplementary Figure 4A]. A noticeable shift toward higher binding energy is observed after FTAC treatment, with the Pb $4f_{7/2}$ and Pb $4f_{5/2}$ peaks moving from 138.02/142.87 eV to 138.15/143.01 eV [Figure 2A]. This is because the ammonium cation in FTAC interacts with the Pb atoms, suggesting the coordination interaction between FTAC and undercoordinated Pb^{2+} ions in the film. The peaks of the I 3d level also shift to higher binding energies after FTAC modification [Figure 2B]. Furthermore, Supplementary Figure 4B and C show the high-resolution Fe 2p spectra collected to verify the successful incorporation of FTAC on the perovskite surface. No detectable Fe signal is observed in the control sample, whereas two characteristic Fe 2p peaks centered at approximately 707.8 and 720.7 eV appear after FTAC treatment, corresponding to the Fe species originating from the ferrocenyl group. The appearance of these characteristic Fe 2p signals provides direct evidence for the presence of FTAC on the perovskite surface.

The role of FTAC in tuning the energy levels of perovskite films was evaluated via UPS. The UPS results, including the secondary-electron cut-off ($E_{cut\text{-}off}$) and the Fermi energy edge region, are presented in Figure 2C. The work functions (WF) of untreated and FTAC-modified perovskite films were determined to be 4.45 eV and 4.55 eV, respectively. The higher WF value after FTAC modification is beneficial for hole extraction and for suppressing charge recombination within the perovskite-HTL interfacial region. The

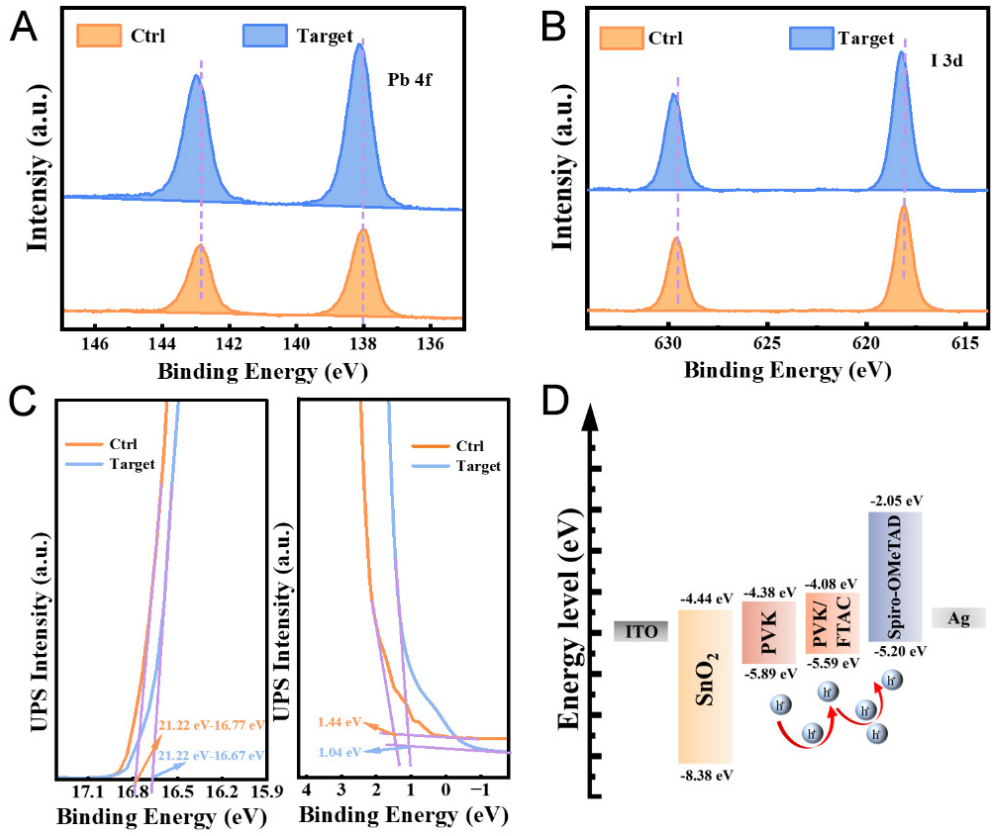

Figure 2. XPS characterization of (A) Pb 4f and (B) I 3d regions for pristine and modified perovskite layers; (C) UPS spectra of the reference and modified perovskite films; (D) Schematic illustration of the energy level structure of the PSC device. FTAC: (Ferrocenylmethyl)trimethylammonium chloride; XPS: X-ray photoelectron spectroscopy; UPS: ultraviolet photoelectron spectroscopy; ITO: indium tin oxide; PVK: perovskite.

energy levels of different perovskite layers are described in Figure 2D and Supplementary Figure 5A based on UPS measurements and Tauc plots [Supplementary Figure 5B]. An upward shift of the valence band maximum from -5.89 eV to -5.59 eV is observed after FTAC treatment, leading to better matching with the HTL. A decreased energy offset between the perovskite absorption layer and the HTL facilitates hole transfer and helps minimize energy loss during their interfacial transport process[39].

In the meantime, Kelvin probe force microscopy (KPFM) was further utilized to probe the surface potential characteristics of perovskite films before and after FTAC modification, as shown in Figure 3A and B. The mean surface potential of FTAC-treated perovskite films was reduced by approximately 58 mV compared with the control sample [Supplementary Table 3]. The sample work function (WF_{sample}) is determined according to[42]:

$$eV_{CPD} = WF_{tip} - WF_{sample} \quad (1)$$

where e denotes the elementary charge, and V_{CPD} represents the contact potential difference between the KPFM tip and the sample. The reduction in the surface potential of the perovskite layer after FTAC treatment indicates an increase in WF, consistent with the trend obtained from UPS measurements. The elevated WF after FTAC modification promotes hole transportation and suppresses nonradiative recombination at the interface with the HTL. Figure 3C and D illustrates the spatial uniformity of the surface potential, which was further analyzed statistically. The surface potential distribution, as characterized by a

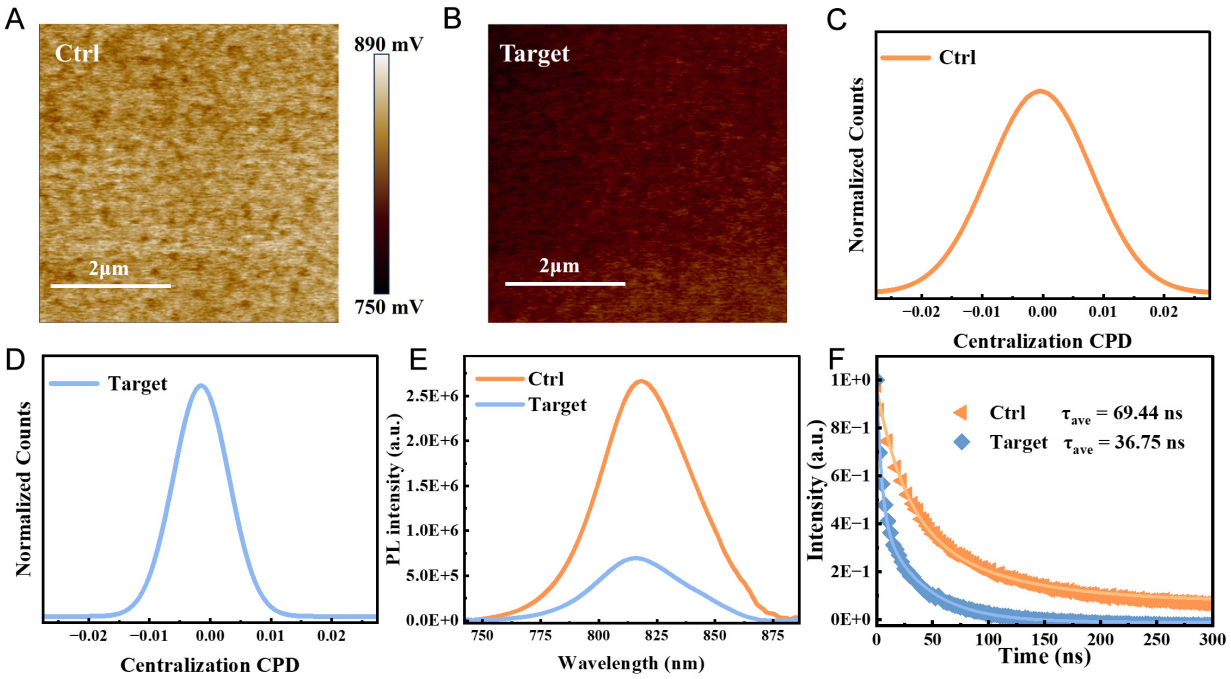

Figure 3. KPFM images of the (A) ctrl perovskite film and (B) target perovskite film. CPD distribution extracted from KPFM data of the (C) ctrl perovskite films and (D) target perovskite films; (E) PL spectra and (F) TRPL decay characteristics of perovskite films with and without FTAC modification (sample structure: ITO/SnO_2/perovskite/HTL and ITO/SnO_2/perovskite/ FTAC/HTL). KPFM: Kelvin probe force microscopy; PL: photoluminescence; TRPL: time-resolved PL; FTAC: (ferrocenylmethyl)trimethylammonium chloride; ITO: indium tin oxide; HTL: hole transport layer; CPD: contact potential difference.

reduction in full width at half maximum (FWHM) from 0.020 to 0.011 after FTAC modification, indicates that the homogeneity of surface potential has been increased due to the reduction in localized charge accumulation[43]. The CPD line-scan profiles in Supplementary Figure 6 also confirmed this result and show a trend consistent with that of the UPS results.

The homogeneity of the surface potential is crucial for promoting efficient charge transport and minimizing interfacial recombination, since a large number of localized charges will capture carriers. PL and TRPL measurements were employed to assess how FTAC treatment influences carrier transport between the perovskite layer and HTL. For these measurements, both the pristine and FTAC treated films were coated onto SnO_2 substrates and overlaid with HTL. In Figure 3E, PL intensity decreases significantly upon FTAC treatment compared with the control sample. The PL intensity values are explicitly indicated on the y-axis, showing that the emission is substantially reduced. This phenomenon can be attributed to the reconstructed perovskite surface formed by FTAC, which reduces interfacial defect states and creates a more homogeneous surface potential distribution. The more uniform potential facilitates interfacial hole transport. In addition, the FTAC-modified surface leads to more favorable energy-level alignment between the perovskite and HTL, thereby facilitating charge extraction. The TRPL decay curves [Figure 3F] were further measured and fitted by a double-exponential decay equation[44]:

$$I(t) = I_0 + A_1 \exp\left(-\frac{t}{\tau_1}\right) + A_2 \exp\left(-\frac{t}{\tau_2}\right) \quad (2)$$

where I is the photoluminescence intensity, t is the time, and τ_1 and τ_2 correspond to the fast and slow decay components. The average carrier lifetime of the FTAC-treated film (36.75 ns) is shorter than that of the control (69.44 ns). The shortened lifetime in the HTL-containing structure suggests that FTAC-induced surface reconstruction effectively promotes hole extraction by simultaneously passivating interfacial defects,

homogenizing the surface potential, and improving the energy-level alignment between the perovskite absorber and HTL. Both the PL and TRPL measurements have shown that FTAC modification can effectively promote charge transfer and suppress charge recombination at the interface. These results arise from the more favorable energy-level alignment and the more homogeneous surface potential distribution across the perovskite layer.

The surface morphology of pristine and FTAC-treated perovskite films was examined by scanning electron microscopy (SEM). As depicted in Figure 4A, the control perovskite film without FTAC treatment exhibited incompletely reacted lead iodide particles on the surface, along with noticeable pores at the grain boundaries. In contrast, the perovskite conversion was more complete following FTAC treatment, with no lead iodide detected on the target perovskite film [Figure 4B]. To further investigate the surface chemical composition of the bright regions observed in the SEM images, XPS analysis was performed on the corresponding films. The detailed fitting results are summarized in Supplementary Table 4. The calculated I/Pb atomic ratios are approximately 5.66 and 5.75 for the control and FTAC-treated films, respectively, indicating that the near-surface region is I-rich rather than Pb-rich. Moreover, no additional Pb 4f chemical component associated with PbI_2 enrichment is detected after FTAC treatment. Therefore, the increased bright contrast in the FTAC-treated film should not be attributed to PbI_2 accumulation, but is more likely related to IPA/DMSO-assisted partial dissolution and FTAC-induced surface reconstruction of the perovskite surface. Cross-sectional SEM images were further collected to evaluate the vertical morphology of the perovskite films [Supplementary Figure 7A and B]. Compared with the control film, the FTAC-treated film exhibits a more compact cross-sectional morphology, and an additional surface layer is observed on top of the optimized perovskite film, indicating the formation of a reconstructed surface region after FTAC treatment. The grain-size distributions of both films are provided in Supplementary Figure 8. The target perovskite film exhibits a narrower grain size distribution, which indicates that the FTAC reconstruction strategy can heal the grain boundaries by dissolving a portion of the smaller grains and promoting the reaction and combination of FTAC with the active surface of the perovskite film[45]. Furthermore, surface elemental mapping via energy-dispersive X-ray spectroscopy (EDS) revealed that the Fe element from FTAC is uniformly distributed on the target perovskite surface, confirming that FTAC homogeneously coats the perovskite thin film surface [Supplementary Figure 9]. This observation is consistent with the high-resolution Fe 2p XPS spectra, providing further evidence for the successful incorporation and uniform distribution of FTAC on the perovskite surface.

The influence of the FTAC reconstruction strategy on the crystallinity of the perovskite layer was investigated by XRD, as shown in Figure 4C. The FTAC-modified films exhibit stronger diffraction peaks at 13.78°, and the areas of the diffraction peaks associated with the (100) and (111) crystal planes were integrated as depicted in Supplementary Table 5. The intensity ratio of (100)/(111) for the target perovskite film increased from 0.99 to 1.87, which contributes to improved hole transport at the perovskite/HTL interface[46]. This increased intensity ratio suggests that FTAC treatment can promote preferential orientation evolution to some extent, mainly in the near-surface region due to its surface post-treatment nature. FTAC primarily regulates the surface and grain-boundary regions through IPA-assisted surface reconstruction rather than inducing complete bulk phase reorientation. More importantly, distinct peaks around 7.1° were observed for the perovskite films treated with FTAC, as shown in Supplementary Figure 10A. The emergence of these diffraction peaks suggests the formation of a two-dimensional perovskite phase, induced by the adsorption of ammonium salt cations onto the perovskite surface through Pb-N bond formation. This two-dimensional layer is advantageous in suppressing surface defects and improving PSC stability[47]. The absorbance spectra of various perovskite samples are presented in Supplementary Figure 10B. These samples exhibited negligible differences because the FTAC reconstruction strategy only affects the shallow surface of perovskite films[48].

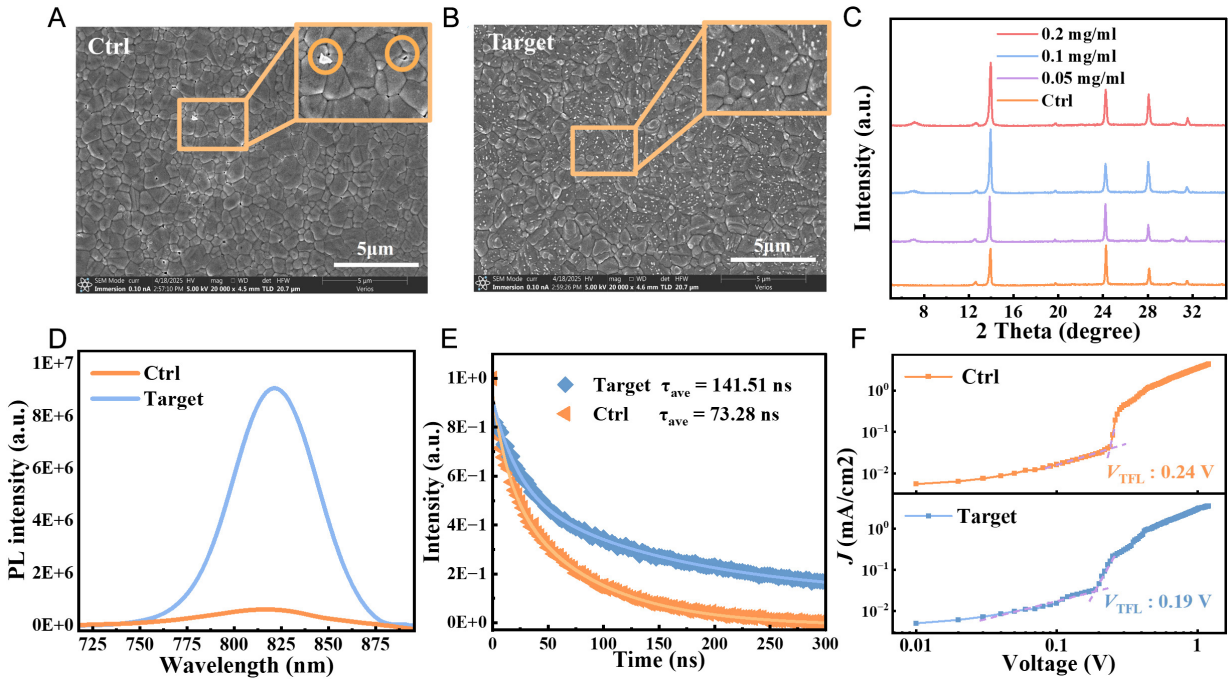

Figure 4. Top-view scanning electron microscopy (SEM) results for (A) the control sample and (B) the target film; (C) XRD patterns of $FAPbI_3$ films treated with varying FTAC concentrations; PL (D) and TRPL (E) spectra of pristine and FTAC-treated perovskite layers; (F) Dark *J-V* characteristics of electron-only devices used to evaluate trap density. XRD: X-ray diffraction; PL: photoluminescence; TRPL: time-resolved PL; FTAC: (ferrocenylmethyl)trimethylammonium chloride; *J-V*: current density-voltage.

The PL and TRPL profiles of perovskite layers fabricated on glass substrates were measured to evaluate the defect density and nonradiative recombination behavior of the perovskite films, as depicted in Figure 4D and E. Compared with the control group, the perovskite film after FTAC reconstruction shows significantly stronger PL intensity. Moreover, the carrier lifetime increased from 73.28 ns to 141.51 ns. Compared with the HTL-containing device in Figure 3F, the FTAC-treated perovskite film without HTL exhibits a much longer average lifetime, confirming that the absence of HTL weakens interfacial hole extraction and leads to slower PL decay. The observed enhancement in PL intensity and carrier lifetime suggests that non-radiative recombination, originating from surface defects in the perovskite films, is effectively suppressed. The density of trap states in the devices was further quantified using SCLC measurements. The electron-only PSC structure is ITO/SnO_2/perovskite/ PCBM/Ag and ITO/SnO_2/perovskite/FTAC/PCBM/Ag. The trap-state density (N_{trap}) can be determined using the following formula[49]:

$$V_{TFL} = \frac{eN_{trap}L^2}{2\varepsilon_0\varepsilon} \quad (3)$$

where V_{TFL} is the trap-filled limit voltage, ε_0 and ε correspond to the vacuum and relative permittivity, respectively, N_{trap} and L represent defect density and the thickness of the perovskite film, respectively. The N_{trap} is determined directly based on the V_{TFL}. As illustrated in Figure 4F, the control and FTAC-modified devices exhibit V_{TFL} values of 0.24 V and 0.19 V, yielding calculated N_{trap} values of 8.49×10^{14} cm^{-3} and 6.72×10^{14} cm^{-3}, respectively. The lowering of N_{trap} is closely associated with improved crystallinity and defect passivation in the perovskite film after FTAC treatment, both of which contribute to the suppression of nonradiative recombination and the resulting enhancement in PSC performance.

As mentioned above, the FTAC reconstruction strategy effectively reduces the localized charges formed at the perovskite film surface by passivating defects, thus yielding a more homogeneous potential profile across the film surface, along with improved energy-level alignment at the perovskite/HTL interface. The n-i-p

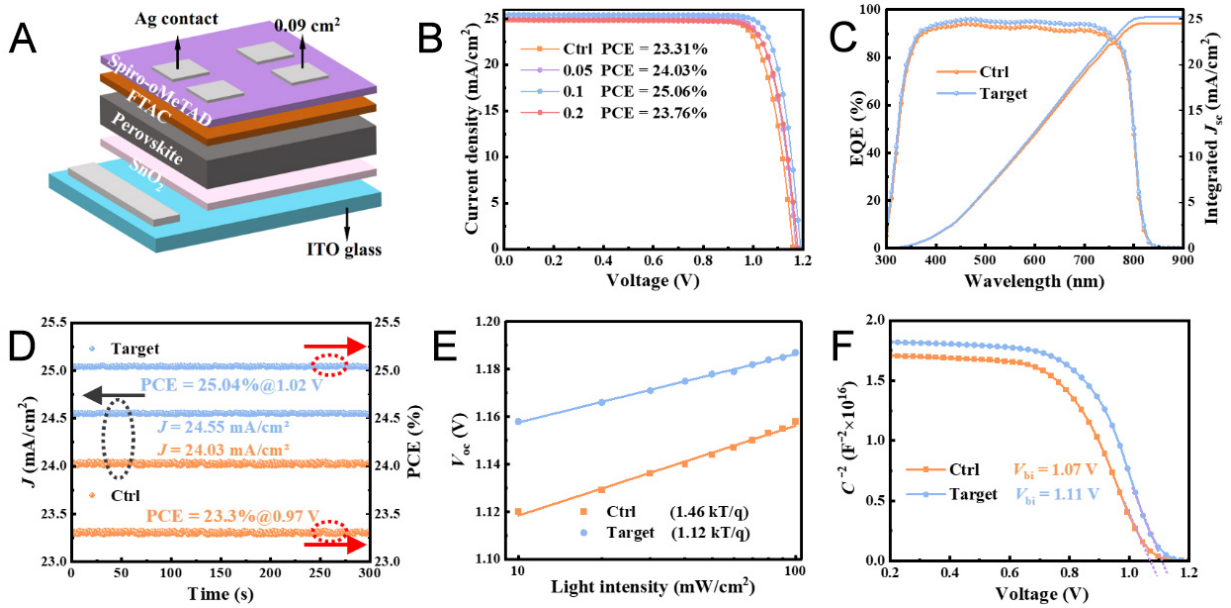

Figure 5. (A) Schematic of the PSC architecture; (B) *J-V* characteristics of optimized PSCs with varying FTAC concentrations; (C) EQE responses and the associated integrated J_{sc} curves of different PSCs; (D) Continuous output performance of different PSCs; (E) Light-intensity-dependent open-circuit voltage of PSCs under 10-100 mW/cm² of different PSCs; (F) Mott-Schottky plots (C^{-2}-V) for various PSCs. FTAC: (Ferrocenylmethyl)trimethylammonium chloride; PCE: power conversion efficiency; PSCs: perovskite solar cells; *J-V*: current density-voltage; EQE: external quantum efficiency; ITO: indium tin oxide.

structured PSCs were fabricated to verify the effect of the FTAC reconstruction strategy on the performance of PSCs [Figure 5A]. Various concentrations ranging from 0.05-0.2 mg/mL of FTAC were utilized to reconstruct the surface of perovskite films. A statistical overview of PSC performance metrics under various conditions is provided in Supplementary Table 6 and Supplementary Figure 11, where each statistical dataset was obtained from 20 independent devices with an active area of 0.09 cm². The device reached its highest performance at an FTAC concentration of 0.1 mg/mL, delivering an average PCE of 24.59%, exceeding that of the control PSCs (22.85%). At a higher FTAC level (0.2 mg/mL), the average PCE declined to 23.29%, likely due to hindered charge transport across the perovskite/HTL interface induced by an overly thick FTAC layer. Figure 5B presents the *J-V* curves of the optimized PSCs, with the corresponding performance metrics summarized in Table 1. The original PSCs demonstrate the highest PCE of 23.31%, characterized by V_{oc} of 1.160 V, short-circuit current density (J_{sc}) of 24.82 mA/cm²· and fill factor (FF) of 80.96%. When the FTAC concentration is 0.1 mg/mL, the modified PSCs deliver the highest PCE of 25.06%, accompanied by V_{oc} of 1.189 V, J_{sc} of 25.41 mA/cm²· and FF of 82.94%. The higher V_{oc} and FF may be attributed to the reduced localized charges, the more homogeneous surface potential, and the enhanced interfacial energy level alignment between the perovskite and HTL, whereas the increase in J_{sc} is likely due to the decreased surface defect density following FTAC modification. Figure 5C shows the EQE spectra along with the corresponding integrated current densities (J_{sc}) for both the original and the 0.1 mg/ml FTAC-treated devices. The target PSC exhibited a higher EQE response compared to the control one, leading to an increase in the integrated J_{sc} from 24.54 mA/cm² to 25.20 mA/cm². The elevated EQE is attributed to the reduction of defects and the more uniform potential distribution at the interface between the perovskite layer and the HTL. The integrated J_{sc} values obtained from EQE curves show good consistency with *J-V* characterization. Under one-sun illumination, the stability of the power output performance of the reference and FTAC-treated PSCs was investigated by applying a bias at the maximum power point, as presented in Figure 5D. Both PSCs demonstrated excellent sustained output capabilities over 300 s, with current densities stabilized at approximately 24.03 mA/cm² and 24.55 mA/cm², respectively. The continuous and stable power output of PSCs is crucial for their commercialization.

Table 1. The best-performance photovoltaic parameters of the control and FTAC-optimized PSCs

Sample	V_{oc} (V)	J_{sc} (mA/cm²)	FF (%)	PCE (%)
Ctrl	1.160	24.82	80.96	23.31
0.05 mg/mL	1.172	24.94	82.21	24.03
Target	1.189	25.41	82.94	25.06
0.2 mg/mL	1.180	24.88	80.92	23.76

FTAC: (Ferrocenylmethyl)trimethylammonium chloride; PSCs: perovskite solar cells; FF: fill factor; PCE: power conversion efficiency.

To further elucidate the recombination mechanism of photogenerated carriers under operational conditions, *J-V* curves were recorded at light intensities ranging from 10 mW/cm² to 100 mW/cm². Figure 5E displays semi-log plots of V_{oc} versus light intensity for different PSCs, with the linear fits expressed as follows[50]:

$$V_{OC} \propto \frac{nkT}{q} lnI \tag{4}$$

where the parameters *n*, *k*, *T*, and *I* refer to the ideality factor, Boltzmann constant, absolute temperature, and illumination intensity, respectively. The *n* values for the control and target PSCs were calculated to be 1.46 and 1.12. The smaller *n* value of the FTAC-modified PSC demonstrates that Shockley-Read-Hall (SRH) recombination at the interface with the HTL is significantly suppressed due to the decreased surface defect density, a more uniform surface potential, and the more suitable energy-level alignment.

Furthermore, the relationship between J_{sc} and light intensity for PSCs presented on a double-log scale was measured [Supplementary Figure 12] and fitted with the power law[51]:

$$J_{SC} \propto I^{\alpha} \tag{5}$$

where α represents the exponential factor. An α value close to 1 indicates that nearly all photogenerated carriers are collected at the electrodes before recombination occurs in the device. The fitted α values for the control and target PSCs were 0.982 and 0.990, which implies that nonradiative recombination is significantly inhibited owing to the diminished defect density and the enhanced surface potential uniformity. The Mott-Schottky (*C-V*) plots were further measured to estimate the built-in electric field (V_{bi}) of different PSCs, as it affects charge separation efficiency and the V_{oc} of PSCs, as presented in Figure 5F. The modified PSC shows a higher V_{bi} of 1.11 V compared to the control device (1.07 V), which aligns well with the V_{oc} enhancement observed in the *J-V* curves. The elevated V_{bi} contributes to more efficient charge separation with decreased recombination. Leakage current in various PSCs was assessed using dark current-voltage characterization, as presented in Supplementary Figure 13. Compared with the control device, the target PSC exhibits a lower dark current, which is associated with fewer surface defects[52].

Thermal stability tests were conducted on epoxy-resin-encapsulated PSCs at 85 °C in a nitrogen environment within a glovebox, based on the ISOS-D-2I standard [Figure 6A]. The target device retained 91.16% of its initial PCE after 1,000 h, showing a marked improvement over the control (42.57%). Additionally, operational stability was evaluated via maximum power point tracking at 65 °C under continuous AM 1.5 illumination (100 mW/cm²), in accordance with ISOS-L-2I protocols. After 1,000 h of continuous operation, the encapsulated target PSC retained 88.67% of its initial efficiency, exceeding the performance of the control device (35.47%), as depicted in Figure 6B. To further evaluate the phase stability of the perovskite films, XRD measurements were performed after 250 h of aging at room temperature [Supplementary Figure 14]. After aging, the PbI_2-related diffraction peak in the control film becomes significantly stronger, whereas it remains relatively weak in the FTAC-treated film, indicating that

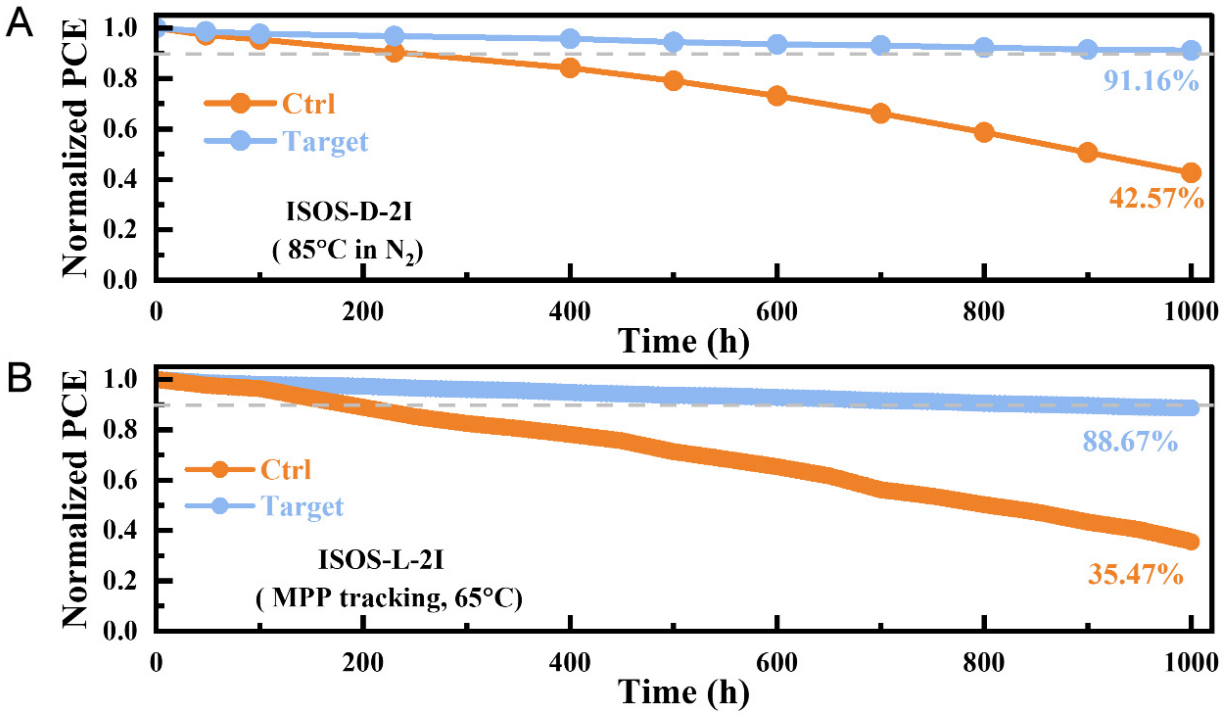

Figure 6. (A) Stability under thermal stress (85 °C) for control and FTAC-modified PSCs in a nitrogen atmosphere glovebox; (B) MPP tracking of these devices at 65 °C in a nitrogen atmosphere, performed based on the ISOS-L-2I standard protocol. FTAC: (Ferrocenylmethyl)trimethylammonium chloride; PSCs: perovskite solar cells; MPP: maximum power point.

FTAC-induced surface reconstruction effectively suppresses phase degradation during aging. The superior stability of the target device is mainly attributed to the suppression of surface defects and the strengthening of the perovskite/HTL interface, which is critical for commercialization.

CONCLUSION

In summary, the FTAC reconstruction strategy aims to reduce localized charges and achieve a uniform surface potential for perovskite films in n-i-p architecture PSCs. The FTAC successfully passivates surface defects through the formation of Pb-N bonds and passivation of iodine vacancies, which suppresses localized charge accumulation and results in a surface with a uniform potential. In addition, FTAC modulates the energy levels of the perovskite layer by reconstructing its surface, thus promoting interfacial charge transport. Consequently, the non-radiative recombination in PSCs is greatly reduced due to decreased surface defect density and more efficient charge transport. The target PSCs exhibit a champion PCE of 25.06%, accompanied by a low V_{oc} loss of 0.32 V. Notably, the optimized PSC retained 91.16% of its initial efficiency after 1000 h of thermal aging at 85 °C and maintained 88.67% after maximum power point (MPP) tracking at 65 °C for the same duration. This work demonstrates a promising route to simultaneously enhance the performance and stability of PSCs by FTAC-induced surface reconstruction of the perovskite film.

DECLARATIONS

Acknowledgments

The XRD, XPS, and SEM characterization data were obtained using equipment maintained by the Analytical and Testing Center, Dongguan University of Technology.

Authors' contribution

Contributed to the experimental design, device fabrication, characterization, data analysis, figure preparation, and manuscript drafting: Chen, R.

Supervised the project, provided financial support, revised the manuscript, and contributed to the

experimental methodology: Zhang, J.
Participated in device fabrication and performance characterization: Luo, Y.
Contributed to the preparation of materials and data analysis: Guo, Z.
Assisted with morphology and structural characterization: Wu, W.
Provided financial support, experimental resources, and research facilities: Xu, X.; Huang, C.; Zhou, H.
All authors discussed the results, reviewed the manuscript, and approved the final version for publication.

Availability of data and materials

The data supporting the findings of this study are available within the article and its Supplementary Materials. Additional data are available from the corresponding author upon reasonable request.

AI and AI-assisted tools statement

During the preparation of this manuscript, the AI tool ChatGPT (GPT-5.5, released 2026-04-23) was used solely for language editing. The tool did not influence the study design, data collection, analysis, interpretation, or the scientific content of the work. All authors take full responsibility for the accuracy, integrity, and final content of the manuscript.

Financial support and sponsorship

This work was financially supported by the National Natural Science Foundation of China (No.62404044), Guangxi Science and Technology Bases and Talent Special Project (No. AD23026132), the Basic and Applied Basic Research Foundation of Guangdong Province (No.2023A1515110062 and No.2023A1515110494), the Guangxi Basic Ability Promotion Project of Middle-aged and Young Teachers in Colleges and Universities (No. 2023KY0205), Director Fund Project of Guangxi Key Laboratory of Optoelectronic Information Processing (No. GD24104), the Guangdong Provincial Key Laboratory Project (High-Performance Integrated Circuits and Systems Laboratory, No.2023KSYS003), and Guangdong Province University Engineering Technology Center (Third-generation semiconductor power chip and application engineering technology Research center, No.2021GCZX008).

Conflicts of interest

All authors declared that there are no conflicts of interest.

Ethical approval and consent to participate

Not applicable.

Consent for publication

Not applicable.

Supplementary Materials

Supplementary Materials

REFERENCES

1. Kojima, A.; Teshima, K.; Shirai, Y.; Miyasaka, T. Organometal halide perovskites as visible-light sensitizers for photovoltaic cells. *J. Am. Chem. Soc.* **2009**, *131*, 6050-1. DOI
2. Zheng, X.; Li, Z.; Zhang, Y.; et al. Co-deposition of hole-selective contact and absorber for improving the processability of perovskite solar cells. *Nat. Energy.* **2023**, *8*, 462-72. DOI
3. You, S.; Zeng, H.; Liu, Y.; et al. Radical polymeric p-doping and grain modulation for stable, efficient perovskite solar modules. *Science* **2023**, *379*, 288-94. DOI
4. Wu, W.; Gao, H.; Jia, L.; et al. Stable and uniform self-assembled organic diradical molecules for perovskite photovoltaics. *Science* **2025**, *389*, 195-9. DOI

5. Ma, B.; Yao, D.; Chen, B.; et al. Thiol groups reutilization on chemical bath deposited tin oxide surface achieving interface anchoring and defects passivation for enhancing the performance and stability of perovskite solar cells. *Small* **2025**, *21*, e2408516. DOI
6. Shi, P.; Ding, Y.; Ding, B.; et al. Oriented nucleation in formamidinium perovskite for photovoltaics. *Nature* **2023**, *620*, 323-7. DOI
7. Li, Y.; Zhang, Z.; Cai, Y.; et al. Synergistic isothiourea-guanidine additive for achieving stable perovskite solar cells with a high certified quasi-steady-state output. *Adv. Mater.* **2026**, *38*, e14903. DOI
8. Yang, Y.; Liu, C.; Ding, Y.; et al. A thermotropic liquid crystal enables efficient and stable perovskite solar modules. *Nat. Energy.* **2024**, *9*, 316-23. DOI
9. Green, M.; Dunlop, E.; Yoshita, M.; et al. Solar cell efficiency tables (Version 66). *Prog. Photovolt. Res. Appl.* **2025**, *33*, 795-810. DOI
10. Yang, B.; Suo, J.; Di Giacomo, F.; et al. Interfacial passivation engineering of perovskite solar cells with fill factor over 82% and outstanding operational stability on n-i-p architecture. *ACS. Energy. Lett.* **2021**, *6*, 3916-23. DOI
11. Li, Y.; Xie, H.; Lim, E. L.; Hagfeldt, A.; Bi, D. Recent progress of critical interface engineering for highly efficient and stable perovskite solar cells. *Adv. Energy. Mater.* **2022**, *12*, 2102730. DOI
12. Oliver, R. D. J.; Caprioglio, P.; Peña-camargo, F.; et al. Understanding and suppressing non-radiative losses in methylammonium-free wide-bandgap perovskite solar cells. *Energy. Environ. Sci.* **2022**, *15*, 714-26. DOI
13. You, S.; Eickemeyer, F. T.; Gao, J.; et al. Bifunctional hole-shuttle molecule for improved interfacial energy level alignment and defect passivation in perovskite solar cells. *Nat. Energy.* **2023**, *8*, 515-25. DOI
14. Duan, H.; Jin, J.; Liu, X.; et al. Electron-donor/-acceptor ratio-guided molecular engineering for buried interface optimization in n-i-p perovskite solar cells. *Energy. Mater.* **2026**, 6. DOI
15. Wang, W. T.; Holzhey, P.; Zhou, N.; et al. Water- and heat-activated dynamic passivation for perovskite photovoltaics. *Nature* **2024**, *632*, 294-300. DOI
16. Ding, B.; Ding, Y.; Peng, J.; et al. Dopant-additive synergism enhances perovskite solar modules. *Nature* **2024**, *628*, 299-305. DOI PubMed PMC
17. Chen, X.; Wang, Q.; Wei, H.; et al. Minimizing the buried interfacial energy loss using a fluorine-substituted small molecule for 25.92%-efficiency and stable inverted perovskite solar cells. *Energy. Environ. Sci.* **2024**, *17*, 7342-54. DOI
18. Shi, X.; Liu, T.; Dou, Y.; et al. Air-processed perovskite solar cells with >25% efficiency and high stability enabled by crystallization modulation and holistic passivation. *Adv. Mater.* **2024**, *36*, e2402785. DOI
19. Zhang, Z.; Chen, W.; Jiang, X.; et al. Suppression of phase segregation in wide-bandgap perovskites with thiocyanate ions for perovskite/organic tandems with 25.06% efficiency. *Nat. Energy.* **2024**, *9*, 592-601. DOI
20. Li, H.; Feng, Y.; Zhu, M.; et al. Nanosurface-reconstructed perovskite for highly efficient and stable active-matrix light-emitting diode display. *Nat. Nanotechnol.* **2024**, *19*, 638-45. DOI
21. Shao, W.; Wang, H.; Fu, S.; et al. Tailoring perovskite surface potential and chelation advances efficient solar cells. *Adv. Mater.* **2024**, *36*, e2310080. DOI
22. Tao, M.; Wang, Y.; Zhang, K.; et al. Molecule-triggered strain regulation and interfacial passivation for efficient inverted perovskite solar cells. *Joule* **2024**, *8*, 3142-52. DOI
23. Pan, Y.; Wang, J.; Sun, Z.; et al. Surface chemical polishing and passivation minimize non-radiative recombination for all-perovskite tandem solar cells. *Nat. Commun.* **2024**, *15*, 7335. DOI PubMed PMC
24. Zhu, X.; Li, M.; Mo, K.; et al. A Surface-reconstructed bilayer heterojunction enables efficient and stable inverted perovskite solar cells. *Adv. Mater.* **2024**, *36*, e2409340. DOI
25. Nie, J.; Zhang, Y.; Wang, J.; Li, L.; Zhang, Y. Recent progress in regulating surface potential for high-efficiency perovskite solar cells. *ACS. Energy. Lett.* **2024**, *9*, 1674-81. DOI
26. Zhou, J.; Bi, E.; Tian, W.; et al. Homogenizing hole-selective contacts for centimeter-square flexible perovskite/Cu(In,Ga)Se_2 tandems. *Sci. Adv.* **2025**, *11*, eadz2781.[DOI:10.1126/sciadv.adz2781.
27. Ou, K.; Liu, J.; Xiang, J.; et al. Importance of passivation efficiency of the passivator for efficient printable mesoscopic perovskite solar cells. *J. Energy. Chem.* **2025**, *106*, 438-45. DOI
28. Xu, Y.; Yu, J.; Liu, S.; et al. Surface potential homogenization improves perovskite solar cell performance. *Adv. Energy. Mater.* **2025**, *15*, 2404755. DOI
29. Huang, H.; Yang, Y.; Liu, B.; et al. Regulating bifacial surface potential of perovskite film enables efficient perovskite solar cells universal for different charge transport layers. *Small* **2025**, *21*, e2412129. DOI
30. Chang, Q.; Wang, F.; Xu, W.; et al. Ferrocene-induced perpetual recovery on all elemental defects in perovskite solar cells. *Angew. Chem. Int. Ed.* **2021**, *60*, 25567-74. DOI
31. Hu, B.; Zhang, J.; Yang, Y.; et al. Tailored multi-functional molecular chain-based ferrocene derivative for efficient and stable perovskite solar cells. *Nano. Energy.* **2023**, *118*, 109022. DOI

32. Vanin, F.; Tremlett, W. D. J.; Gao, D.; et al. Modulating perovskite surface energetics through tuneable ferrocene interlayers for high-performance perovskite solar cells. *Angew. Chem. Int. Ed.* **2025**, *64*, e202424041. DOI
33. Webb, T.; Liu, X.; Westbrook, R. J.; et al. A multifaceted ferrocene interlayer for highly stable and efficient lithium doped spiro-OMeTAD-based perovskite solar cells. *Adv. Energy. Mater.* **2022**, *12*, 2200666. DOI
34. Perdew, J. P.; Burke, K.; Ernzerhof, M. Generalized gradient approximation made simple. *Phys. Rev. Lett.* **1996**, *77*, 3865-8. DOI PubMed
35. Kresse, G.; Furthmüller, J. Efficient iterative schemes for ab initio total-energy calculations using a plane-wave basis set. *Phys. Rev. B. Condens. Matter.* **1996**, *54*, 11169-86. DOI PubMed
36. Kresse, G.; Joubert, D. From ultrasoft pseudopotentials to the projector augmented-wave method. *Phys. Rev. B.* **1999**, *59*, 1758-75. DOI
37. Oner, S. M.; Sezen, E.; Yordanli, M. S.; Karakoc, E.; Deger, C.; Yavuz, I. Surface defect formation and passivation in formamidinium lead triiodide ($FAPbI_3$) perovskite solar cell absorbers. *J. Phys. Chem. Lett.* **2022**, *13*, 324-30. DOI PubMed
38. Yang, S.; Zhuang, Y.; Dou, Y.; et al. Investigation of the effect of molecules containing sulfonamide moiety adsorbed on the $FAPbI_3$ perovskite surface: a first-principles study. *Molecules* **2025**, *30*, 2463. DOI PubMed PMC
39. Xia, J.; Sohail, M.; Nazeeruddin, M. K. Efficient and stable perovskite solar cells by tailoring of interfaces. *Adv. Mater.* **2023**, *35*, e2211324. DOI PubMed
40. Tao, J.; Zhao, C.; Wang, Z.; et al. Suppressing non-radiative recombination for efficient and stable perovskite solar cells. *Energy. Environ. Sci.* **2025**, *18*, 509-44. DOI
41. Jiang, Q.; Zhu, K. Rapid advances enabling high-performance inverted perovskite solar cells. *Nat. Rev. Mater.* **2024**, *9*, 399-419. DOI
42. Lu, Y.; Zhong, J.; Yu, Y.; et al. Constructing an n/n^+ homojunction in a monolithic perovskite film for boosting charge collection in inverted perovskite photovoltaics. *Energy. Environ. Sci.* **2021**, *14*, 4048-58. DOI
43. Li, Z.; Li, B.; Wu, X.; et al. Organometallic-functionalized interfaces for highly efficient inverted perovskite solar cells. *Science* **2022**, *376*, 416-20. DOI
44. Zhang, Y.; Yu, B.; Sun, Y.; Zhang, J.; Su, Z.; Yu, H. An MBene modulating the buried SnO_2/perovskite interface in perovskite solar cells. *Angew. Chem. Int. Ed.* **2024**, *63*, e202404385. DOI
45. Chen, H.; Teale, S.; Chen, B.; et al. Quantum-size-tuned heterostructures enable efficient and stable inverted perovskite solar cells. *Nat. Photon.* **2022**, *16*, 352-8. DOI
46. Masi, S.; Gualdrón-reyes, A. F.; Mora-seró, I. Stabilization of black perovskite phase in $FAPbI_3$ and $CsPbI_3$. *ACS. Energy. Lett.* **2020**, *5*, 1974-85. DOI
47. Teale, S.; Degani, M.; Chen, B.; Sargent, E. H.; Grancini, G. Molecular cation and low-dimensional perovskite surface passivation in perovskite solar cells. *Nat. Energy.* **2024**, *9*, 779-92. DOI
48. Wang, H.; Zhang, Z.; Wang, X.; Duan, L.; Luo, J. Phenyltrimethylammonium chloride additive for highly efficient and stable $FAPbI_3$ perovskite solar cells. *Nano. Energy.* **2024**, *123*, 109423. DOI
49. Zhang, J.; Yu, H. Multifunctional dopamine-assisted preparation of efficient and stable perovskite solar cells. *J. Energy. Chem.* **2021**, *54*, 291-300. DOI
50. Lin, Y.; Lin, Z.; Lv, S.; et al. A Nd@C_{82}-polymer interface for efficient and stable perovskite solar cells. *Nature* **2025**, *642*, 78-84. DOI
51. Zhao, C.; Wang, F.; Hu, X.; et al. Ambient blade-coated perovskite solar cells with high reverse bias stability enabled by polymeric hole transporter design. *Nat. Commun.* **2025**, *16*, 10355. DOI PubMed PMC
52. Xu, Y.; Wu, Z.; Zhang, Z.; Li, X.; Lin, H. Evolved photovoltaic performance of $MAPbI_3$ and $FAPbI_3$-based perovskite solar cells in low-temperatures. *Energy. Mater.* **2024**, *4*, 400034. DOI